



HAL
open science

Mixing and bottom friction: parameterization and application to the surf zone

Anne-Claire Bennis, Franck Dumas, Fabrice Ardhuin, Bruno Blanke

► To cite this version:

Anne-Claire Bennis, Franck Dumas, Fabrice Ardhuin, Bruno Blanke. Mixing and bottom friction: parameterization and application to the surf zone. 2012. hal-00681292v1

HAL Id: hal-00681292

<https://hal.science/hal-00681292v1>

Preprint submitted on 21 Mar 2012 (v1), last revised 24 Apr 2014 (v2)

HAL is a multi-disciplinary open access archive for the deposit and dissemination of scientific research documents, whether they are published or not. The documents may come from teaching and research institutions in France or abroad, or from public or private research centers.

L'archive ouverte pluridisciplinaire **HAL**, est destinée au dépôt et à la diffusion de documents scientifiques de niveau recherche, publiés ou non, émanant des établissements d'enseignement et de recherche français ou étrangers, des laboratoires publics ou privés.

Mixing and bottom friction: parameterization and application to the surf zone

ANNE-CLAIRE BENNIS*

*Université de Bretagne Occidentale, Laboratoire de Physique des Océans,
UMR 6523 CNRS-Ifremer-IRD-UBO, 29200 Brest, France.*

FRANCK DUMAS

Ifremer, DYNECO/PHYSED, Centre de Brest, 29200 Plouzané, France.

FABRICE ARDHUIN

Ifremer, Laboratoire d'Océanographie Spatiale, Centre de Brest, 29200 Plouzané, France.

BRUNO BLANKE

CNRS, Laboratoire de Physique des Océans, UMR 6523 CNRS-Ifremer-IRD-UBO, 29200 Brest, France.

* *Corresponding author address:* Anne-Claire Bennis, Laboratoire de Physique des Océans, 29200 Brest.

ABSTRACT

Wave breaking has been observed to affect the bottom boundary layer in surf zones, with potential impacts on bottom friction. The present paper investigates the impact of wave breaking on bottom friction and set-up using a recently proposed parameterization of the wave-induced turbulent kinetic energy in turbulent closure equations of the wave-averaged flow. The behavior of this parameterization is investigated by comparing phase-resolving and phase-averaged solutions. We show that the phase-averaged solution strongly overestimates turbulent kinetic energy, in a way similar to the modeling of air flow over waves. The current is correctly simulated. When applied to a realistic planar beach and after some modifications, the mixing parameterization yields the correct reproduction of the observed longshore current, with only a limited impact on wave set-up.

1. Introduction

Waves in the nearshore zone drive morphodynamic and hydrodynamic responses at many spatial and temporal scales (e.g. Svendsen 2006). The most obvious hydrodynamic features are the longshore currents (Bowen 1969) and the increase in mean sea level on the shoreface (e.g. Longuet-Higgins and Stewart 1963). In the first case, the magnitude of the current is inversely proportional to bottom friction (e.g. Longuet-Higgins 1970), and friction is believed to be a secondary term in the cross-shore momentum balance, in which the wave-induced momentum flux divergence is mostly balanced by the hydrostatic pressure gradient associated with the wave set-up (e.g. Apotsos et al. 2007).

An accurate parameterization of friction is thus the first priority when modeling surf

zone flows. For this reason, many in situ experiments have tried to determine some physical roughness parameter, and various studies aimed at estimating meaningful friction coefficients from observed flow patterns (Feddersen et al. 2000, 2003). These studies have suggested that friction may not only be a function of bottom roughness, but may also depend on wave breaking. There are some other possible sources of discrepancy between roughness and friction coefficients, including some differences in roughness between the alongshore and cross-shore directions, on account of specific form drags over bedforms (e.g. Barrantes and Madsen 2000), or the multiple velocity time scales that must be accounted when investigating the effect of bottom friction on either of the flow components (e.g., the effects of waves on the dissipation of infragravity waves in Reniers et al. 2002). Our purpose here is thus to investigate a possible parameterization of wave breaking effects on bottom friction, by adding breaking-induced turbulence in the phase-averaged mixing parameterization proposed by Mellor (2002) (ML02, hereafter) for modeling of the bottom boundary layer. This parameterization uses turbulent kinetic energy to represent the influence of wave-induced near-bottom turbulence on the mean flow, and was shown to reproduce accurately observed current profiles.

The parameterization and its application to an oscillatory bottom boundary layer are described in section 2. Its application to a realistic surf zone is presented in section 3. Conclusions follow in section 4.

2. The phase-averaged parameterization and its application to an oscillatory boundary layer

In this section, we simulate the oscillations of the wave bottom boundary layer with the wave phase for a one-dimensional vertical (1DV) case, and we compare the outcome with that based on phase-averaged simulations. We redo the numerical experiment described by Mellor (2002) to compare our results with his model data and with laboratory data from Jensen et al (1989). Next, we test the behavior of the phase-averaged parameterization when the waves break, by parameterizing the effects of wave breaking.

a. The governing equations

When the wave phase is solved, the momentum equations in terrain-following coordinates are the same as eqs. (9a) and (9b) in Mellor (2002), except that we use a k-epsilon closure to parameterize vertical mixing instead of the Mellor and Yamada (1982)'s scheme. The differences between both turbulent schemes have little impact on the results of this study.

$$\frac{\partial u}{\partial t} = \frac{\tau_{0x}}{h} + u_{bx}\omega\cos(\omega t) + \frac{1}{D} \frac{\partial \tau_x}{\partial \zeta}, \quad (1)$$

$$\frac{\partial k}{\partial t} = \frac{1}{D^2} \cdot \frac{\partial}{\partial \zeta} \left(\frac{\nu_V}{s_k} \cdot \frac{\partial k}{\partial \zeta} \right) - \frac{\partial k}{\partial \zeta} \cdot \frac{\partial \zeta}{\partial t} + \text{Prod} + \text{Buoy} - \epsilon, \quad (2)$$

$$\frac{\partial \epsilon}{\partial t} = \frac{1}{D^2} \cdot \frac{\partial}{\partial \zeta} \left(\frac{\nu_V}{s_\epsilon} \cdot \frac{\partial \epsilon}{\partial \zeta} \right) - \frac{\partial \epsilon}{\partial \zeta} \cdot \frac{\partial \zeta}{\partial t} + \frac{\epsilon}{k} (c_1 \text{Prod} + c_3 \text{Buoy} - c_2 \epsilon). \quad (3)$$

where u is the flow velocity in the x-direction, k is the turbulent kinetic energy (TKE, hereafter), ϵ is the dissipation rate, D is the mean depth and $h = D/2$, ζ is the terrain-

following coordinate and t stands for time.

The mixing length is given by $l = (c_\mu^0)^3 k^{3/2} \epsilon^{-1}$ with $0.5270 \leq c_\mu^0 \leq 0.5544$ and the vertical viscosity is $\nu_V = l(2k)^{1/2} S_M$ (where S_M is the stability function¹).

The wave forcing is induced by the pressure gradient, $u_{bx}\omega\cos(\omega t)$, with a velocity amplitude $u_{bx} = 2 \text{ m.s}^{-1}$ and a wave frequency $\omega = 0.654 \text{ s}^{-1}$. The mean flow is generated by a force analogous to a pressure gradient τ_{0x}/h , where $\tau_{0x} = 4.10^{-3} \text{ m}^2.\text{s}^{-2}$ is the x-component of the mean wall stress vector and h is equal to 0.14 m. The term τ_x is the x-component of the Reynolds stress. In equations (2) and (3), c_1 , c_2 and c_3 are constant parameters. The terms 'Prod' and 'Buoy' are related to TKE and dissipation production by shear and buoyancy; the 'Buoy' term is set to zero in our case.

The parameterization of Mellor (2002) deals with the phase-averaged flow. Then, the following momentum equations are solved where $\overline{(\cdot)}$ denotes phase-averaged quantities:

$$\frac{\partial \bar{u}}{\partial t} = \frac{\bar{\tau}_{0x}}{h} + \frac{1}{D} \frac{\partial \bar{\tau}_x}{\partial \zeta}, \quad (4)$$

$$\frac{\partial \bar{k}}{\partial t} = \frac{1}{D^2} \cdot \frac{\partial}{\partial \zeta} \left(\frac{\bar{\nu}_V}{s_k} \cdot \frac{\partial \bar{k}}{\partial \zeta} \right) - \frac{\partial \bar{k}}{\partial \zeta} \cdot \frac{\partial \zeta}{\partial t} + \overline{\text{Prod}} + \overline{\text{Buoy}} - \bar{\epsilon} + \bar{P}_k, \quad (5)$$

$$\frac{\partial \bar{\epsilon}}{\partial t} = \frac{1}{D^2} \cdot \frac{\partial}{\partial \zeta} \left(\frac{\bar{\nu}_V}{s_\epsilon} \cdot \frac{\partial \bar{\epsilon}}{\partial \zeta} \right) - \frac{\partial \bar{\epsilon}}{\partial \zeta} \cdot \frac{\partial \zeta}{\partial t} + \frac{\bar{\epsilon}}{k} (c_1 \overline{\text{Prod}} + c_3 \overline{\text{Buoy}} - c_2 \bar{\epsilon} F_{wall}) + \bar{P}_{eps}. \quad (6)$$

Two production source terms (\bar{P}_k and \bar{P}_{eps}) are added in the standard equations for the k-epsilon model, with the following forms:

$$\bar{P}_k = \omega u_b^2 (F_{1\Phi} F_{2z})^3, \quad (7)$$

¹The quasi-equilibrium form of Kantha and Clayson (1994) is used. The stability function is derived algebraically from the transport equations for the Reynolds stresses.

$$\overline{P}_{eps} = C \frac{\bar{\epsilon}}{\bar{k}} P_k. \quad (8)$$

where \overline{P}_k , $F_{1\Phi}$ and F_{2z} are given in Mellor (2002) by equations (18), (20) and (21a), respectively. F_{2z} is a function of depth distributing the source terms over the water column. C is a non-dimensional constant equal to 0.9337. u_b is the magnitude of the orbital velocity.

In order to correctly model the oscillations of the bottom boundary layer, the expression of the bottom shear stress must be modified. Our formulation lies on the near-bottom TKE, so that the effects of the additional terms of TKE can be incorporated. This formulation is not based on a drag coefficient like in the classical equations. The expression of the wave-averaged bottom shear stress ($\bar{\tau}_{bx}$) depends on the ratio z/z_0 , where z_0 is the bottom roughness and z is the depth from the bottom. If $z > z_0$, we use the following expression

$$\bar{\tau}_{bx} = \frac{\bar{u}\kappa S_{M0} \sqrt{2\bar{k}_0}}{\ln\left(\frac{z}{z_0}\right)}. \quad (9)$$

If $0 < z \leq z_0$, and to suppress undesirable effects of a negative bottom shear stress, we rather use:

$$\bar{\tau}_{bx} = \frac{\bar{u}\kappa S_{M0} \sqrt{2\bar{k}_0}}{\ln\left(\frac{z}{z_0} + 1\right)}. \quad (10)$$

where \bar{k}_0 is the wave-averaged turbulent kinetic energy near the bottom, κ is the Von Kármán constant set to 0.4 and the stability function S_{M0} takes the value 0.39 in the absence of stratification.

b. Validation: Pure oscillatory flow

Before analyzing the results of the phase-averaged cases, we compare our model results for the oscillatory boundary layer with the vertical current profiles measured in laboratory

by Jensen et al. (1989) and the numerical results of Mellor (2002) for this example. We set $\tau_{0x} = 0 \text{ m}^2 \cdot \text{s}^{-2}$ in equation (1) in order to simulate a pure oscillatory flow. The resulting flow is oscillating in time, varying with the wave phase (Ψ) given by relation $\Psi = \frac{360 \cdot t}{T}$ (where T is the oscillatory period set to 9.6 s). When the flow is established (ie. when the transition stage is over), we study only half a wave period (with phases between 0° and 180°) because the flow is symmetric. We choose to simulate a rough wall with a bottom roughness set to $2.8 \cdot 10^{-5} \text{ m}$, which has the value considered in the simulations run by Mellor (2002).

Our simulations are carried out with a one-dimensional version of the MARS3D code (Lazure and Dumas 2008), using a very high vertical resolution (3600 regularly distributed levels, so that the vertical resolution is about $7.7 \cdot 10^{-5} \text{ m}$), which ensures a good representation of near bottom processes but does not resolve bottom roughness. We use a time step equal to 0.005 s. Figure 1 (top row) shows the vertical profiles of the current for the accelerating $0 \leq \Psi < 90^\circ$ and decelerating $90 \leq \Psi < 180^\circ$ phases of the flow. Our results are similar to the measured profiles and to the model results reported by Mellor (2002) (see Figure 1). In particular, the oscillations of the bottom boundary layer are correctly reproduced. The vertical profiles of TKE (see Figure 1, middle row) are also comparable to the observed ones and to the numerical results by Mellor (2002), with some differences that we attribute to the use of a different turbulence scheme and a different vertical resolution. However, very close to the bottom, our results obtained in the case of a rough surface slightly differ from the observations. Both models strongly overestimate the level of TKE near the boundary. This may be related to the way we apply the wave forcing (i.e. an oscillatory barotropic pressure gradient), which differs from the experimental conditions of Jensen et al. (1989) (i.e. oscillatory flows in a vein). Moreover, Jensen et al. (1989) use a smooth wall for their

experiment. Lastly, the bottom shear stress computed by Mellor (2002) is shown for each wave phase in Figure 1 (bottom row, blue circles), for an easy comparison with our results (red crosses). The results are similar.

c. Fully developed mean flow superimposed on an oscillatory flow

1) IMPACT OF THE VERTICAL DISCRETIZATION

We consider a fully developed mean flow superimposed on oscillatory flow. The mean flow is generated by the terms $\frac{\tau_{0x}}{h}$ and $\frac{\bar{\tau}_{0x}}{h}$, that are now non-zero and set to $2.10^{-3} \text{ m}^2.\text{s}^{-2}$. As in Mellor (2002), we consider for this case a depth equal to 4 m. In order to correctly simulate the flow for this depth, we use a vertical mesh that is refined near the bottom and near the surface. In practice, the vertical discretization has a large influence on the near-bottom value of F_{2z} (see Appendix A, eq. (A11)), which may strongly modify the solution. Five meshes have been used to reveal this problem (more details in Appendix A, eq. (A11)), with some of them including grid points within the bottom roughness (Mesh 3 and 4). For each individual mesh, the depth of the grid point nearest the bottom (z_{bot}) and the corresponding value of F_{2z} are given in Table 1. The near-bottom value of the F_{2z} function varies between 0.2 and 5 according to the mesh (see Figure 2, top row). Indeed, when $z \rightarrow 0$, both the F_{2z} function goes to infinity, which has a non-negligible influence on the vertical profile of the current. For smaller z_{bot} values, the near-bottom source of TKE is increased and the vertical current shear is reduced. After many numerical experiments, we found that $F_{2z} \simeq 1$ reproduces reasonably well the average of the phase-resolving solution. Our final experiment uses mesh No. 5 with a modified F_{2z} function ($F_{2z,mod}$) for which all values greater than 1

are reset to values close to unity such that $F_{2z,mod} = \min(F_{2z}, 1)$ (see Figure 2, right panel, blue curve). Moreover, we suppress all negatives values as recommended by Mellor (2002) in order to add only turbulent source terms. The depth-integrated value of F_{2z} , for the different meshes, is modified by the suppression of all the negative values and, therefore, the turbulent quantities that are injected differ.

When the waves do not break, the vertical profile of the current given by the phase-averaged parameterization is very close to the profile obtained in the phase-resolving case (see Figure 3, NO BREAK case). The TKE values near the bottom are greatly increased for the phase-averaged case (see Figure 4, NO BREAK case) because the parameterization uses additional sources of turbulent kinetic energy (\overline{P}_k) and turbulent dissipation (\overline{P}_ϵ) that are maximum near the bottom. TKE is about three times larger than in the phase-resolving case. This high value is reminiscent of the difficulties encountered with mixing length models used for the simulation of air flow over waves. Indeed, the oscillations due to waves are known to prevent the turbulent mixing when the eddy overturning time becomes larger than the wave period (Belcher and Hunt 1993). In these conditions, the classical mixing length models, in particular when applied to the phase-averaged flow, generally fail to reproduce this effect and overestimate the mixing (Miles 1996), in the outer boundary layer.

In both cases, when a steady state is reached, the depth-averaged pressure gradient balances the bottom stress, which is thus the same in phase-resolving and phase-averaged simulations.

2) EFFECTS OF WAVE BREAKING

We anticipate the use of the phase-averaged parameterization in realistic surf zones where waves break. As a preliminary study, we apply it on the previous test case, where we assess the effects of wave breaking at the surface. These effects are parameterized. We account for additional sources of TKE and turbulent dissipation, linearly distributed over a characteristic length δ according to Walstra et al (2000). Both terms depend on wave energy dissipation resulting from wave breaking (D_w), such that $D_w = 6.75 \cdot 10^{-4} \text{ m}^3 \cdot \text{s}^{-3}$ (and $\rho_0 D_w = 0.69 \text{ W} \cdot \text{m}^{-2}$, where ρ_0 is the reference water density set to $1027 \text{ kg} \cdot \text{m}^{-3}$).

The additional source terms for TKE (P_{kbr} and \bar{P}_{kbr}) are the same in both phase-averaged and phase-resolving cases, and we test two vertical distributions determined by a characteristic length δ :

- Case 1: $\delta = 0.5 \cdot H_{\text{rms}} \simeq 1 \text{ m}$:

$$P_{kbr} = \bar{P}_{kbr} = \frac{4D_w}{H_{\text{rms}}} \left(1 - \frac{2z'}{H_{\text{rms}}} \right). \quad (11)$$

- Case 2: $\delta = \frac{11 \cdot H_{\text{rms}}}{8} \simeq 3 \text{ m}$:

$$P_{kbr} = \bar{P}_{kbr} = \frac{16D_w}{11H_{\text{rms}}} \left(1 - \frac{8z'}{11H_{\text{rms}}} \right). \quad (12)$$

where z' is the distance from the surface and H_{rms} is the root mean square significant wave height.

For both values of δ , the depth-integrated value of P_{kbr} is the same, and is equal to D_w . The additional source of turbulent dissipation (P_{ebr}) is computed from the source of TKE. For the phase-resolved case, we have

$$P_{ebr} = 1.44 \cdot P_{kbr} \cdot \left(\frac{\epsilon}{k} \right), \quad (13)$$

and for the phase-averaged case, we use the following expression

$$\bar{P}_{ebr} = 1.44 \cdot \bar{P}_{kbr} \cdot \left(\frac{\bar{\epsilon}}{\bar{k}} \right). \quad (14)$$

The surface boundary conditions for the k-epsilon model must be changed to account for wave breaking at the surface. A Dirichlet boundary condition is used for TKE (Kantha and Clayson 2004):

$$k_{z'=0} = \bar{k}_{z'=0} = B_1^{2/3} [1 + 3mb\alpha]^{2/3} u_*^2. \quad (15)$$

where B_1 , b , m , and α are non-dimensional constants set to 16.6, 0.22, 1, and 100, respectively. u_* is the friction velocity.

At the surface, we use a flux boundary condition for turbulent dissipation following Burchard (2001):

* For the phase-resolved case:

$$\frac{\partial \epsilon}{\partial z} \Big|_{z'=0} = (c_\mu^0)^{3/4} \left[\frac{\frac{3}{2} \cdot \frac{\sigma_k (c_\mu^0)^{3/4} c_w u_*^3}{c_\mu} + \kappa k^{3/2}}{\kappa^2 (z' + z_{0s})^2} \right]. \quad (16)$$

* For the averaged-resolved case:

$$\frac{\partial \bar{\epsilon}}{\partial z} \Big|_{z'=0} = (c_\mu^0)^{3/4} \left[\frac{\frac{3}{2} \cdot \frac{\sigma_k (c_\mu^0)^{3/4} c_w u_*^3}{c_\mu} + \kappa \bar{k}^{3/2}}{\kappa^2 (z' + z_{0s})^2} \right]. \quad (17)$$

where c_μ^0 , c_μ , c_w , σ_k are non-dimensional constants, equal to 0.09, 0.09, 100, and 1, respectively. z_{0s} is the surface roughness that we set to $0.6 \cdot H_s$ (where H_s is the significant

wave height). We note that for $c_w = 0$, we obtain the flux boundary conditions for non-breaking case.

For both characteristic lengths of breaking penetration, the effects of wave breaking do not reach the bottom of the water column. Therefore, turbulent kinetic energy near the bottom is not modified (see Figure 4, BREAK: case 1 and case 2). However, wave breaking homogenizes TKE over most of the water column in comparison with the NO BREAK case. Moreover, as the depth-integrated value of P_{kbr} is the same for both cases with wave breaking, the vertical profiles of TKE are similar. The depth-integrated TKE in case 2 is only 0.9% greater than in case 1, most probably because of numerical effects induced by the refined vertical mesh. With a regular vertical mesh, the depth-integrated TKE should be the same for both cases. The TKE budget (see Figure 5) shows that the production terms (Prod. in figure 5) balance the dissipation (Diss. in figure 5) and diffusion (Diff. in figure 5) terms. Besides TKE production by shear, the production terms include the sources related to wave breaking and to the Mellor (2002) parameterization. The mixing induced by wave breaking reduces the vertical shear of the current and decreases the magnitude of velocity in the corresponding regions. The deeper the penetration of mixing, the smaller the surface velocity (see Figure 3, BREAK: case 1 and case 2). However, in both present cases, the effects of wave breaking on current are weak.

To conclude, for all cases, with and without wave breaking, the phase-averaged parameterization correctly reproduces the current while it overestimates near-bottom turbulent kinetic energy, in comparison with the phase-resolving case. Moreover, the parameterization shows good performance in presence of wave breaking at the surface. We can apply it now to surf zones.

3. Bottom friction and wave set-up in a surf zone

Apostos et al (2007) showed that for shallow depths less than 30 centimeters, the wave set-up phenomenon is poorly reproduced by the current numerical models. For these depths, the mixing caused by wave breaking interacts with the mixing enhanced by bottom friction. Apostos et al (2007) consider that these interactions may modify bottom friction and impact on the set-up. The parameterization of Mellor (2002) allows computation of the bottom shear stress from the turbulent kinetic energy and is relevant to study such effects of wave breaking. Therefore, we use the phase-averaged parameterization previously tested to quantify, in a surf zone, the modification of the bottom shear stress by wave breaking and the consequences on the computed longshore current and set-up.

We use the MARS3D-WAVEWATCH III coupled model (Bennis et al, 2011) based on the quasi-Eulerian velocity (the Lagrangian velocity minus the Stokes velocity). This coupled model allows to simulate three-dimensional flows in presence of waves by the full coupling of one wave model, WAVEWATCH III (Tolman, 2009 and Ardhuin et al, 2010), with one regional ocean circulation model, MARS 3D (Lazure et Dumas, 2008). Hereafter, we remind the momentum equations in terrain-following coordinates (more details in Bennis et al (2011) and Ardhuin et al (2008)). Note that all variables introduced in this section are phase-averaged, so the previous notation $(\bar{\cdot})$ is removed for sake of readability.

$$\begin{aligned}
 \frac{\partial \hat{u}}{\partial t} &+ \hat{u} \frac{\partial \hat{u}}{\partial x} + \hat{v} \frac{\partial \hat{u}}{\partial y} + \hat{W} \frac{\partial \hat{u}}{\partial \zeta} - f \hat{v} + \frac{1}{\rho} \left(\frac{\partial p^H}{\partial x} + \frac{\partial p^H}{\partial \zeta} \cdot \frac{\partial \zeta}{\partial x} \right) \\
 &= \left[f + \left(\frac{\partial \hat{v}}{\partial x} + \frac{\partial \hat{v}}{\partial \zeta} \cdot \frac{\partial \zeta}{\partial x} \right) \right] V_s - \left(\frac{\partial \hat{u}}{\partial y} + \frac{\partial \hat{u}}{\partial \zeta} \cdot \frac{\partial \zeta}{\partial y} \right) V_s \\
 &\quad - \frac{W_s}{D} \cdot \frac{\partial \hat{u}}{\partial \zeta} - \frac{\partial J}{\partial x} - \frac{\partial J}{\partial \zeta} \cdot \frac{\partial \zeta}{\partial x} + \hat{F}_{d,x} + \hat{F}_{m,x} + \hat{F}_{b,x},
 \end{aligned} \tag{18}$$

$$\begin{aligned}
\frac{\partial \widehat{v}}{\partial t} &+ \widehat{u} \frac{\partial \widehat{v}}{\partial x} + \widehat{v} \frac{\partial \widehat{v}}{\partial y} + \widehat{W} \frac{\partial \widehat{v}}{\partial \zeta} + f \widehat{u} + \frac{1}{\rho} \left(\frac{\partial p^H}{\partial y^*} + \frac{\partial p^H}{\partial \zeta} \cdot \frac{\partial \zeta}{\partial y} \right) \\
&= - \left[f + \left(\frac{\partial \widehat{v}}{\partial x} + \frac{\partial \widehat{v}}{\partial \zeta} \cdot \frac{\partial \zeta}{\partial x} \right) \right] U_s + \left(\frac{\partial \widehat{u}}{\partial y} + \frac{\partial \widehat{u}}{\partial \zeta} \cdot \frac{\partial \zeta}{\partial y} \right) U_s \\
&\quad - \frac{W_s}{D} \cdot \frac{\partial \widehat{v}}{\partial \zeta} - \frac{\partial J}{\partial y} - \frac{\partial J}{\partial \zeta} \cdot \frac{\partial \zeta}{\partial y} + \widehat{F}_{d,y} + \widehat{F}_{m,y} + \widehat{F}_{b,y}.
\end{aligned} \tag{19}$$

where $(\widehat{u}, \widehat{v}, \widehat{w})$ is the quasi-Eulerian velocity, p^H is the hydrostatic pressure, $(\widehat{F}_{m,x}, \widehat{F}_{m,y})$ are the mixing effects induced by waves and other processes, $(\widehat{F}_{d,x}, \widehat{F}_{d,y})$ are the sources of quasi-Eulerian momentum that are equal to the sink of wave momentum induced by wave breaking and wave-turbulence interaction, $(\widehat{F}_{b,x}, \widehat{F}_{b,y})$ are the sources of quasi-Eulerian momentum related to the sink of wave momentum induced by bottom friction (to be included only when the wave bottom boundary layer is resolved), J is the wave-induced mean pressure and (U_s, V_s, W_s) is the three-dimensional Stokes drift.

Two evolution equations (one for TKE, one for turbulent dissipation) are used for modeling turbulence:

$$\frac{\partial k}{\partial t} = \frac{1}{D^2} \cdot \frac{\partial}{\partial \zeta} \left(\frac{\nu_V}{s_k} \cdot \frac{\partial k}{\partial \zeta} \right) - \frac{\partial k}{\partial \zeta} \cdot \frac{\partial \zeta}{\partial t} + \text{Prod} + \text{Buoy} - \epsilon + \mathcal{P}_k, \tag{20}$$

$$\frac{\partial \epsilon}{\partial t} = \frac{1}{D^2} \cdot \frac{\partial}{\partial \zeta} \left(\frac{\nu_V}{s_\epsilon} \cdot \frac{\partial \epsilon}{\partial \zeta} \right) - \frac{\partial \epsilon}{\partial \zeta} \cdot \frac{\partial \zeta}{\partial t} + \frac{\epsilon}{k} (c_1 \text{Prod} + c_3 \text{Buoy} - c_2 \epsilon) + \mathcal{P}_\epsilon. \tag{21}$$

Equations (20) and (21) are the classical equations of the k-epsilon model with the addition of two source terms, \mathcal{P}_k and \mathcal{P}_ϵ , accounting for the mixing effects due to bottom friction and wave breaking. These terms differ according to the simulated test cases and are given by equations (22) and (23). For the parameterization of Mellor (2002), the constant β is set to one and the constant γ is set to zero. For the other case, the constants β and γ are equal to zero and one, respectively.

$$\mathcal{P}_k = \frac{4D_w}{H_{rms}} \left(1 - \frac{2z'}{H_{rms}}\right)_{z' \leq H_{rms}/2} + \beta\omega |\mathbf{u}_b|^2 (F_{1\psi} F_{2z})^3 + \gamma \frac{2D_f}{\delta} \left(1 - \frac{D-z'}{\delta}\right)_{D-\delta \leq z' \leq D} \quad (22)$$

$$\begin{aligned} \mathcal{P}_\epsilon &= \frac{\epsilon}{k} \left[1.44 \left(\frac{4D_w}{H_{rms}} \left(1 - \frac{2z'}{H_{rms}}\right)_{z' \leq H_{rms}/2} + \gamma \frac{2D_f}{\delta} \left(1 - \frac{D-z'}{\delta}\right)_{D-\delta \leq z' \leq D} \right) \right] \quad (23) \\ &+ \frac{\epsilon}{k} [C\beta\omega |\mathbf{u}_b|^2 (F_{1\psi} F_{2z})^3]. \end{aligned}$$

where δ is the thickness of the wave bottom boundary layer, D_f is the wave energy dissipation due to bottom friction (calculated from Soulsby (1995) and based on a cubic near-bottom wave orbital velocity), z' is the distance from the surface and D is the mean depth. The dissipation due to wave breaking, D_w , directly comes from the wave model.

The original function F_{2z} given by Mellor (2002) shows some problems for this case. As discussed in the previous section, the near-bottom values change according to the mesh in use, with numerical inaccuracy as a result. Here, a strange behavior of F_{2z} is obtained because the values of the wave orbital velocity near the bottom are weaker than for the 1DV case. The wave orbital velocities are less than $0.75 \text{ m}\cdot\text{s}^{-1}$, which leads to positive values of F_{2z} near the surface (see Figure 6, top row). Indeed, when the near-bottom wave orbital velocity goes to zero, F_{2z} goes to infinity at the surface (see Appendix A, eq. (A11)). These positive values introduce some turbulent kinetic energy near the surface, which is not physically realistic because F_{2z} must monotonously decrease from the bottom to the surface. Unphysical interaction with wave breaking is another problem. Therefore, we remove from now on all unrealistic positive values of F_{2z} near the surface in addition to its negative values (see Figure 6, bottom row).

By analogy with the previous study, we change the surface boundary condition for TKE into the following Dirichlet boundary condition (Burchard 2001):

$$k = \frac{(u_\star)^2}{c_\mu^{1/2}} \left[a + \left(\frac{3\sigma_k}{2} \right)^{1/2} c_\mu^{1/4} c_w \right]^{2/3} \quad (24)$$

where a is set to one. The other constants have been previously defined.

WAVEWATCH III, the wave model that solves the transport equation of the wave action density spectrum N (N being function of time, space, wave number and direction), is a phase-averaged model.

$$\frac{DN}{Dt} = \frac{S}{\sigma} \quad (25)$$

where S represents the source terms and σ is the intrinsic wave radian frequency.

As the wave model does not solve the wave phase, the expression of bottom shear stress must account for the oscillations of the wave bottom boundary layer with the wave phase. Parameterizations for the bottom shear stress classically use the wave orbital velocity near the bottom. It is the case for the Soulsby (1995) parameterization that we will test hereafter. The formulation of Mellor (2002) is another type of parameterization that is based on near-bottom TKE. We compare here the results given by Mellor (2002) (ML02, hereafter) with the results given by Walstra et al (2000) with the Soulsby (1995) parameterization (WSB95, hereafter) for modeling near-bottom processes. For the WSB95 case, the additional source terms are given by eq. (22) and (23) with $\beta = 0$ and $\gamma = 1$, and the bottom shear stress (\mathcal{T}_t) is expressed as:

$$\mathcal{T}_t = \mathcal{T}_c \left[1 + 1.2 \left(\frac{|\mathcal{T}_w|}{|\mathcal{T}_w| + |\mathcal{T}_c|} \right)^{3.2} \right], \quad (26)$$

where \mathcal{T}_c and $|\mathcal{T}_w|$ are the bottom shear stresses due to the current and to the waves, respectively:

$$\mathcal{T}_c = \rho_0 \left[\frac{\kappa}{\log\left(\frac{z_m}{z_0}\right)} \right]^2 |\hat{\mathbf{u}}_1| |\hat{\mathbf{u}}_1| \quad \text{and} \quad |\mathcal{T}_w| = \frac{1}{2} \rho_0 f_w |\mathbf{u}_{\text{orb}}|^2. \quad (27)$$

z_m is a reference depth above the sea bed, \mathbf{u}_{orb} is the wave orbital velocity near the bottom, ρ_0 is the reference density, $\hat{\mathbf{u}}_1 = (\hat{u}_1, \hat{v}_1)$ is the quasi-Eulerian velocity near the bottom and f_w is a wave friction factor (Soulsby, 1997) defined as:

$$f_w = 1.39 \left(\frac{\sigma z_0}{|\mathbf{u}_{\text{orb}}|} \right)^{0.52}. \quad (28)$$

The formulations are tested in the Nearshore Sediment Transport Study (NSTS) configuration (Wu et al, 1985 and Thornton and Guza, 1986). An incident oblique wave is propagating on a planar beach (Leadbetter beach in California). The bathymetry decreases with the cross-shore distance, and a longshore current and breaking waves develop (see Figure 7). The main characteristics of the wave forcing are the following: the significant wave height is less than one meter ($\simeq 0.96$ m), the mean wave period is about twelve seconds and the mean wave direction is about 109 degrees. As we have an incidence angle of 19 degrees, the southern boundary (treated like a wall) casts a shadow in the model domain (Figure 8). This shadow is removed in the coupled model by the use of a smaller computational domain for MARS3D and the use of periodic boundary conditions at its northern and southern boundaries.

For both models, the time step is set to one second and the horizontal resolution is $4\text{m} \times 20\text{m}$. We use a refined vertical mesh near the bottom and near the surface, with 100 sigma levels (i.e., $\lambda t = 100$), allowing the resolution of the bottom roughness set to $2 \cdot 10^{-3}$ m. The expression of the vertical mesh is the following (where λ represents the vertical grid

point and λ_{max} , here set to 1200, is the number of grid points distributed over the entire water column)

$$\varsigma = a_1 \cdot \exp [a_2 \cdot (\lambda - \lambda t)] + a_3, \quad \varsigma < \lambda t/2, \quad (29)$$

$$\varsigma = -a_1 \cdot \exp [-a_2 \cdot (\lambda - 1)] + a_4 \cdot \exp [0.5 \cdot a_2(1 - \lambda t)] + a_5, \quad \varsigma \geq \lambda t/2. \quad (30)$$

with $a_1 = 9.67 \cdot 10^3$, $a_2 = 0.2$, $a_3 = -0.99$, $a_4 = 1.93 \cdot 10^4$ and $a_5 = -0.97$.

The depth (z''), equal to the mean sea surface elevation $\hat{\eta}$ at the surface and to $-h$ at the bottom, is computed as:

$$z'' = \varsigma \cdot (\hat{\eta} + h) + \hat{\eta}. \quad (31)$$

Longuet-Higgins (1970) showed that in the longshore direction, the bottom shear stress balances the barotropic longshore current. Thus, we evaluate the validity of our computed bottom shear stress by using the measurements of the barotropic longshore current. The wave forcing is correctly simulated (see Figure 9, top row). For a bottom roughness set to $2 \cdot 10^{-3} m$, which is coherent with a sandy beach (Feddersen and Trowbridge 2005), the peak of the barotropic longshore current computed for the WSB95 case has an intensity similar to the observed one (see Figure 9, WSB95 case). However, this peak is located nearer the shore than the observed one because the bottom stress formulation is probably unsuitable for this case. Indeed, the parameterization of Soulsby (1995) does not account for the mixing effects induced by wave breaking, though this process directly impacts on the spatial location of the peak of the current. Moreover, this parameterization has been deduced from model and data intercomparison and, therefore, it can induce some inaccuracies on the results.

We now test the ML02 parameterization with the modified F_{2z} (see previous explanations)

to possibly improve the simulation of the barotropic longshore current. The comparison with NSTS data shows that the simulated maximum longshore current is now about three times weaker than the observed one, due to the overestimation of the bottom shear by the ML02 parameterization (see Figure 9, bottom row, original ML02 case). In ML02, the bottom shear stress in the y-direction depends only on two parameters, the near-bottom turbulent kinetic energy (k_0) and the bottom roughness (z_0) because the bottom shear stress in the y-direction (τ_{by}) can be expressed as:

$$\tau_{by} = A \cdot \hat{v}, \quad (32)$$

where:

* If $z > z_0$,

$$A = \frac{\kappa S_{M0} \sqrt{2k_0}}{\ln\left(\frac{z}{z_0}\right)}. \quad (33)$$

* If $0 < z \leq z_0$,

$$A = \frac{\kappa S_{M0} \sqrt{2k_0}}{\ln\left(\frac{z}{z_0} + 1\right)}. \quad (34)$$

For the WSB95 case, the A term is equal to:

$$A = \left[\frac{\kappa}{\log\left(\frac{z_m}{z_0}\right)} \right]^2 \cdot \left[1 + 1.2 \left(\frac{|\mathcal{T}_w|}{|\mathcal{T}_w| + |\mathcal{T}_c|} \right)^{3.2} \right] \cdot |\hat{\mathbf{u}}_1| \quad (35)$$

These equations show the very different scalings of the two bottom stresses, with one based on near-bottom TKE and one other based on the near-bottom wave orbital velocity.

Although the bottom roughness is relatively uncertain, a reasonable current is only obtained with z_0 as small as 1.10^{-4} m, which is about one order of magnitude smaller than the

value estimated for similar sandy beaches (e.g. Feddersen and Trowbridge (2005)).

The A term, plotted for all parameterizations in Figure 10, balances the current in the bottom stress parameterization. The A term is about four times larger in the ML02 case (Figure 10, bottom row, left panel, original ML02 case) than in the WSB95 case, which induces a weaker barotropic longshore current. This term in ML02, for fixed z and z_0 , only depends on the near-bottom TKE. Therefore, its overestimation is caused by an inappropriate level of TKE near the bottom, which is similar to what we found when comparing the phase-resolving and phase-averaged models.

If bottom friction is defined using eq. (32) with a TKE level reduced by a factor 2, the magnitude of the longshore current becomes acceptable (see Figure 9, modified ML02 case). The comparison with WSB95 shows that the modified ML02 gives a good location for the peak of the longshore current, highlighting the positive impact induced by the account of TKE in the bottom stress parameterization. Alternatively, we may reduce the values of F_{2z} in order to leave unchanged the possible input of TKE from breaking waves. However, this would adversely modify the current profile.

Lastly, we find that the way we model bottom stress does not affect much the set-up (see Figure 11). Many numerical simulations show that the wave set-up is significantly increased when bottom friction is strongly increased.

4. Summary and Conclusions

In this study, we investigated the relevance of a bottom friction parameterization based on turbulent kinetic energy, with sources naturally included from the wave bottom boundary

layer and wave breaking, following the work of Mellor (2002). For this purpose, we specified the profile of a phase-averaged source of near-bottom TKE and we corrected some weaknesses in the profile parameterization proposed by Mellor (2002). Although the mean current profile can be reproduced, the model strongly overestimates TKE near the bottom. The additional source of TKE related to breakers at the surface (Walstra et al 2000) has minimal impact on the vertical profile of the current and the ML02 parameterization shows a good behavior in presence of waves breaking. Two characteristic lengths were tested to distribute the wave breaking sources over depth. We obtained almost similar results, knowing that some differences are due to the need for a refined vertical mesh near the bottom and near the surface. The TKE equilibrium differs according to the characteristic length used for the distribution of the turbulent sources induced by wave breaking. In all cases, the production terms balance the dissipation and diffusion terms.

Then, for a surf zone, we compared the parameterization of Mellor (2002) with an equivalent scheme that was proposed by Walstra et al (2000) and embeds Soulsby's (1995) parameterization. The parameterization of Soulsby (1995) for bottom stress does not consider the effects of mixing induced by wave breaking because it is only based on the wave orbital velocity near the bottom. Here, the vertical structure of the F_{2z} function must be changed because, otherwise, the orbital velocity in use adds unrealistic turbulent kinetic energy and dissipation near the surface. Moreover, by comparison with the NSTS data, the bottom shear stress computed with the original parameterization of Mellor (2002) was shown to produce a weaker longshore current. Trial simulations were used to find that an acceptable longshore current is obtained if one divides by two the near-bottom level of TKE. Then, we note that the location of the peak of the longshore current is in agreement with the obser-

vations. Therefore, we conclude that the use of the near-bottom TKE in the bottom stress parameterization is relevant, and we recommend the modification of the parameterization of Mellor (2002) before its use in a surf zone.

Acknowledgments.

A-C. B. acknowledges the support of a post-doctoral grant from UBO (Université de Bretagne Occidentale), and from the PREVIMER and IOWAGA projects. F.A. is supported by a FP7-ERC grant #240009 “IOWAGA”.

APPENDIX A

(i) *Some vertical meshes*

The discrete vertical distribution for the terrain-following coordinate (ς) is the following for each mesh (where λ represents the vertical grid point and λ_{max} , here set to 1200, is the number of grid points distributed over the entire water column):

* Mesh 1:

$$\varsigma = \frac{\exp(0.001265 \cdot \lambda)}{2.3} - 1.428, \quad \varsigma < \lambda_{max}/2, \quad (\text{A1})$$

$$\varsigma = \frac{-\exp(0.001265 \cdot (-\lambda + \lambda_{max}))}{2.3} + 0.43, \quad \varsigma \geq \lambda_{max}/2. \quad (\text{A2})$$

* Mesh 2:

$$\varsigma = \frac{\exp(0.01265 \cdot \lambda)}{3.98 \cdot 10^3} - 0.999, \quad \varsigma < \lambda_{max}/2, \quad (\text{A3})$$

$$\varsigma = \frac{-\exp(0.01265 \cdot (-\lambda + \lambda_{max}))}{3.98 \cdot 10^3} - 0.005, \quad \varsigma \geq \lambda_{max}/2. \quad (\text{A4})$$

* Mesh 3:

$$\varsigma = \frac{\exp(0.03 \cdot \lambda)}{1.28 \cdot 10^8} - 1, \quad \varsigma < \lambda_{max}/2, \quad (\text{A5})$$

$$\varsigma = \frac{-\exp(0.03 \cdot (-\lambda + \lambda_{max}))}{1.28 \cdot 10^8}, \quad \varsigma \geq \lambda_{max}/2. \quad (\text{A6})$$

* Mesh 4:

$$\varsigma = \frac{\exp(0.02 \cdot \lambda)}{3.2 \cdot 10^5} - 1, \quad \varsigma < \lambda_{max}/2, \quad (\text{A7})$$

$$\varsigma = \frac{-\exp(0.02 \cdot (-\lambda + \lambda_{max}))}{3.2 \cdot 10^5}, \quad \varsigma \geq \lambda_{max}/2. \quad (\text{A8})$$

* Mesh 5:

$$\varsigma = \frac{\exp(0.017 \cdot \lambda)}{7.49 \cdot 10^3} - 0.999, \quad \varsigma < \lambda_{max}/2, \quad (\text{A9})$$

$$\varsigma = \frac{-\exp(0.017 \cdot (-\lambda + \lambda_{max}))}{7.49 \cdot 10^3}, \quad \varsigma \geq \lambda_{max}/2. \quad (\text{A10})$$

The elevation from the bottom (z) is given by: $z = 2h\varsigma + 2h$.

The F_{2z} function is given in Mellor (2002) (see his equation (21a)) and his expression is recalled hereafter.

$$\begin{aligned} F_{2z} = & -0.0488 + 0.02917lz + 0.01703lz^2 \\ & + [1.125(lz_0 + 5) + 0.125(lz_0 + 5)^4] \times (-0.0102 - 0.00253lz + 0.00273lz^2) \end{aligned} (\text{A11})$$

with $lz = \ln\left(\frac{z\omega}{u_b}\right)$ and $lz_0 = \log\left(\frac{z_0\omega}{u_b}\right)$

REFERENCES

- Apotsos, A., B. Raubenheimer, S. Elgar, R. T. Guza, and J. A. Smith, 2007: Effects of wave rollers and bottom stress on wave setup. *J. Geophys. Res.*, **112**, C02 003, doi:10.1029/2006JC003549.
- Barrantes, A. I. and O. S. Madsen, 2000: Near-bottom flow and flow resistance for currents obliquely incident to two-dimensional roughness elements. *J. Geophys. Res.*, **105 (C11)**, 26 253–26 264.
- Belcher, S. E. and J. C. R. Hunt, 1993: Turbulent shear flow over slowly moving waves. *J. Fluid Mech.*, **251**, 109–148.
- Bowen, A. J., 1969: The generation of longshore currents on a plane beach. *J. Mar. Res.*, **27**, 206–215.
- Burchard, H., 2001: Simulating the wave-enhanced layer under breaking surface waves with two-equation turbulence models. *J. Phys. Oceanogr.*, **31**, 3133–3145.
- Feddersen, F., E. L. Gallagher, R. T. Guza, and S. E. Feddersen, 2003: The drag coefficient, bottom roughness, and wave-breaking in the nearshore. *Coastal Eng.*, **48**, 189–195.
- Feddersen, F., R. T. Guza, S. Elgar, and T. H. C. Herbers, 2000: Velocity moments in alongshore bottom stress parameterizations. *J. Geophys. Res.*, **105 (C4)**, 8673–8686.

- Feddersen, F. and J. H. Trowbridge, 2005: The effect of wave breaking on surf-zone turbulence and alongshore currents: a modelling study. *J. Phys. Oceanogr.*, **35**, 2187–2204.
- Jensen, B. L., B. M. Sumer, and J. Fredsøe, 1989: Turbulent oscillatory boundary layers at high Reynolds numbers. *J. Fluid Mech.*, **206**, 265–297.
- Kantha, L. H. and C. A. Clayson, 1994: An improved mixed layer model for geophysical applications. *J. Geophys. Res.*, **99**, 25 235–25 266.
- Kantha, L. H. and C. A. Clayson, 2004: On the effect of surface gravity waves on mixing in the oceanic mixed layer. *Ocean Modelling*, **6**, 101–124.
- Lazure, P. and F. Dumas, 2008: An external-internal mode coupling for a 3d hydrodynamical model for applications at regional scale (MARS). *Adv. Water Resources*, **31**, 233–250.
- Longuet-Higgins, M. S., 1970: Longshore currents generated by obliquely incident sea waves, 2. *J. Geophys. Res.*, **75**, 6790–6801.
- Longuet-Higgins, M. S. and R. W. Stewart, 1963: A note on wave set-up. *J. Mar. Res.*, **21**, 4–10.
- Mellor, G., 2002: Oscillatory bottom boundary layers. *J. Phys. Oceanogr.*, **32**, 3075–3088.
- Mellor, G. L. and T. Yamada, 1982: Development of a turbulence closure model for geophysical fluid problems. *Rev. Geophys. Space Phys.*, **20 (C2)**, 851–875.
- Miles, J., 1996: Surface wave generation: a viscoelastic model. *J. Fluid Mech.*, **322**, 131–145.

Reniers, A. J. H. M., A. R. van Dongeren, J. A. Battjes, and E. B. Thornton, 2002: Linear modeling of infragravity waves during delilah. *J. Geophys. Res.*, **107 (C10)**, 3137, doi: 10.1029/2001JC001083.

Svendsen, I., 2006: *Introduction to nearshore hydrodynamics*. World Scientific, Singapore, 722 pp.

List of Tables

- 1 Near-bottom values of z and F_{2z} according to the mesh in use. 28

	z_{bot}	F_{2z}^{bot}
Mesh 1	$3 \cdot 10^{-2}$ m	0.2
Mesh 2	$9.2 \cdot 10^{-4}$ m	0.9
Mesh 3	$3.2 \cdot 10^{-8}$ m	5.5
Mesh 4	$1.3 \cdot 10^{-5}$ m	2.4
Mesh 5	$7.6 \cdot 10^{-5}$ m	1.8

TABLE 1. Near-bottom values of z and F_{2z} according to the mesh in use.

List of Figures

- 1 Vertical profiles of current (top row) and turbulent kinetic energy (middle row) for wave phases between 0° and 165° obtained with the MARS model. Bottom row: comparison of bottom shear stress between the MARS results (red crosses) and Mellor(2002) results (blue circles) for all wave phases. 31
- 2 Left panel: different vertical meshes and the depending function F_{z2} . All meshes include 1200 grid points distributed over the entire water column, and only every fifth step is kept in the figure for clarity. Right panel: F_{z2} function for mesh number 5. The original function as given by ML02 is in red and our modified function is in blue. 32
- 3 Comparison of vertical velocity profiles for cases with and without waves breaking at the surface (NO BREAK: without waves breaking, BREAK: case 1 and 2 are for $\delta \simeq 1$ m and for $\delta \simeq 3$ m, respectively). Results given by the phase-resolving case (INST) are compared with the results given by the phase-averaged case (ML02). 33
- 4 Comparison of TKE vertical profiles for cases with and without waves breaking at the surface (NO BREAK: without waves breaking, BREAK: case 1 and 2 are for $\delta \simeq 1$ m and for $\delta \simeq 3$ m, respectively). Results given by the phase-resolving case (INST) are compared with the results given by the phase-averaged case (ML02). 34

- 5 TKE budget for the ML02 parameterization. The production terms (Prod),
the dissipation terms (Diss) and the diffusion terms (Diff) are plotted as a
function of depth. The top row shows the entire water column down to a
depth of fifty centimeters. The bottom row shows the first five centimeters.
Cases with and without wave breaking at the surface are displayed. 35
- 6 F_{2z} function for different cross-shore positions. The original F_{2z} function given
by ML02 (top row) and our modified function (bottom row). 36
- 7 Cross-shore profiles of bathymetry (top row), root mean square significant
wave height (middle row) and barotropic longshore current (bottom row). All
these profiles come from measurements made during the NSTS experiment. 37
- 8 Map of the significant wave height computed by WAVEWATCH III. The
gray zone shows the computational domain used for the hydrodynamic model
(MARS3D). 38
- 9 Comparison between observational data and the model for the significant wave
height (top row) and the barotropic longshore current (bottom row), with
results from different parameterizations. 39
- 10 Comparison between the modified ML02, the original ML02 and the WSB95
parameterizations for TKE (top row, left panel), the y-component of the bot-
tom shear stress (top row, right panel), the term A (bottom row, left panel)
and the 3D longshore velocity near the bottom (bottom row, right panel). 40
- 11 Comparison of the mean sea surface elevation for the modified ML02, the
original ML02, and the WSB95 parameterizations. 41

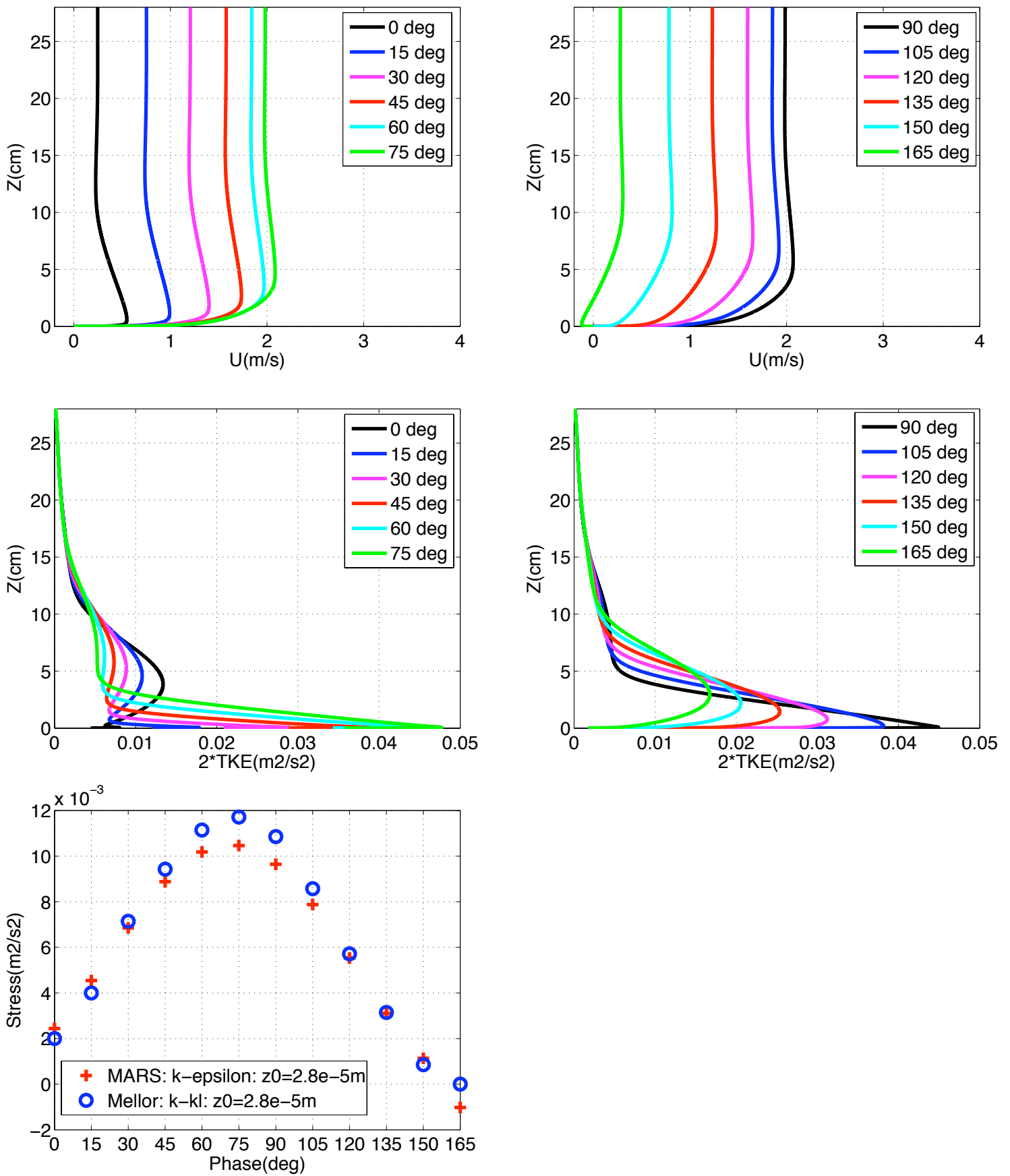


FIG. 1. Vertical profiles of current (top row) and turbulent kinetic energy (middle row) for wave phases between 0° and 165° obtained with the MARS model. Bottom row: comparison of bottom shear stress between the MARS results (red crosses) and Mellor(2002) results (blue circles) for all wave phases.

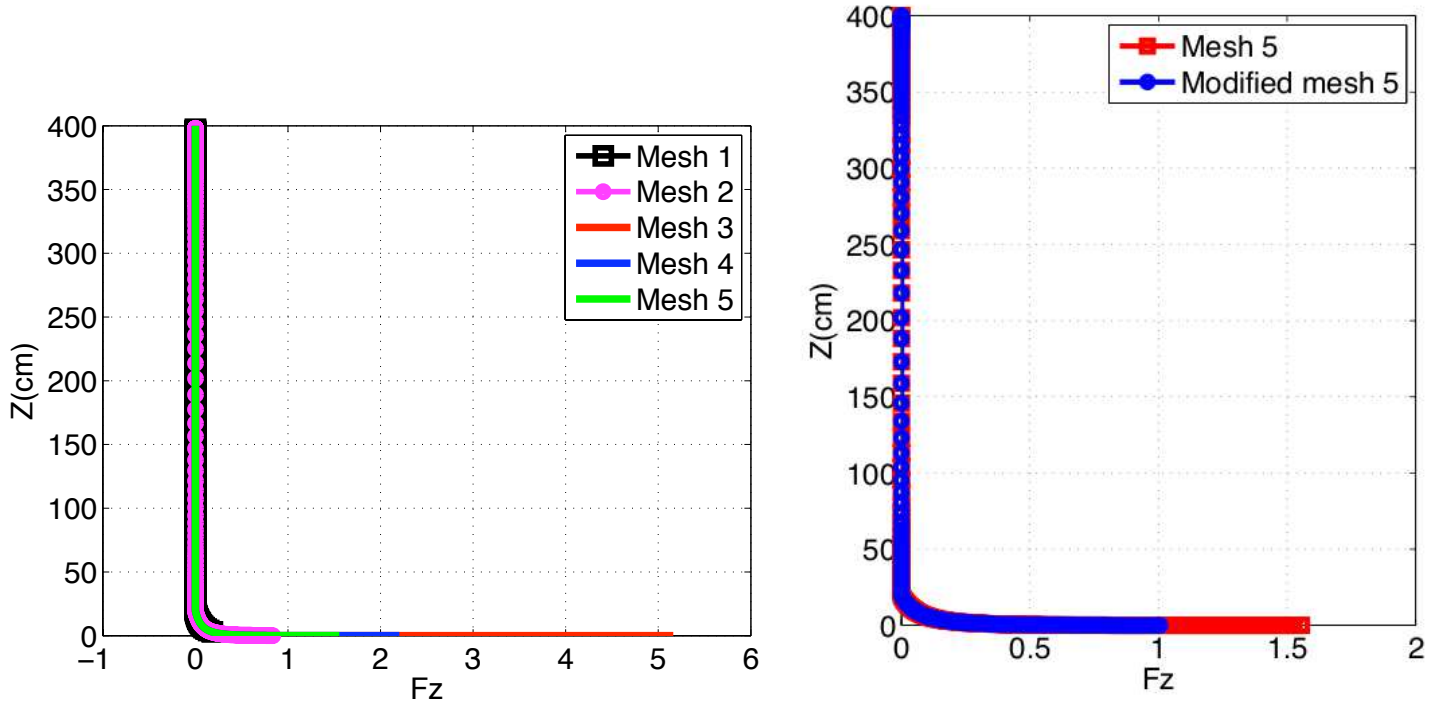


FIG. 2. Left panel: different vertical meshes and the depending function F_{z2} . All meshes include 1200 grid points distributed over the entire water column, and only every fifth step is kept in the figure for clarity. Right panel: F_{z2} function for mesh number 5. The original function as given by ML02 is in red and our modified function is in blue.

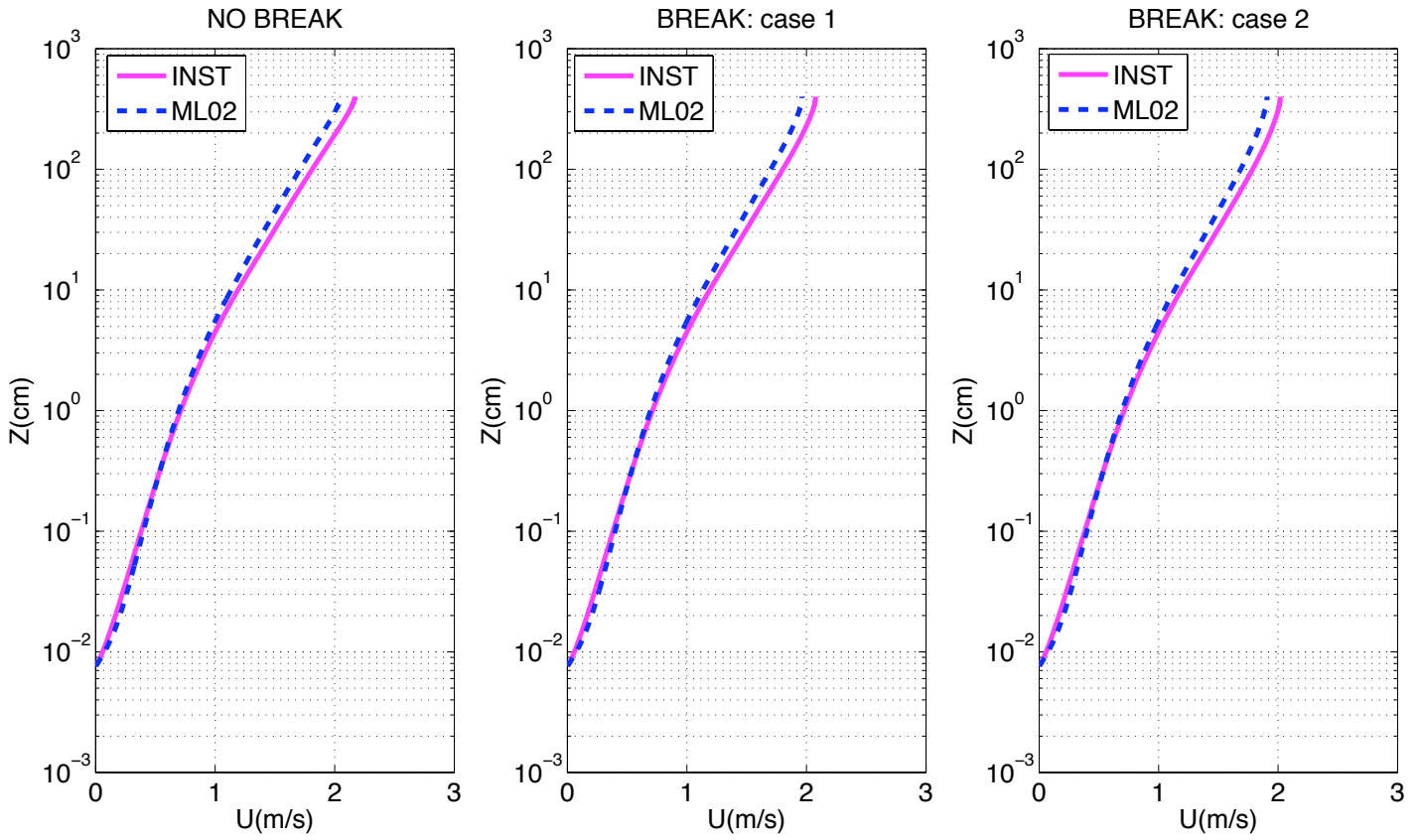


FIG. 3. Comparison of vertical velocity profiles for cases with and without waves breaking at the surface (NO BREAK: without waves breaking, BREAK: case 1 and 2 are for $\delta \simeq 1$ m and for $\delta \simeq 3$ m, respectively). Results given by the phase-resolving case (INST) are compared with the results given by the phase-averaged case (ML02).

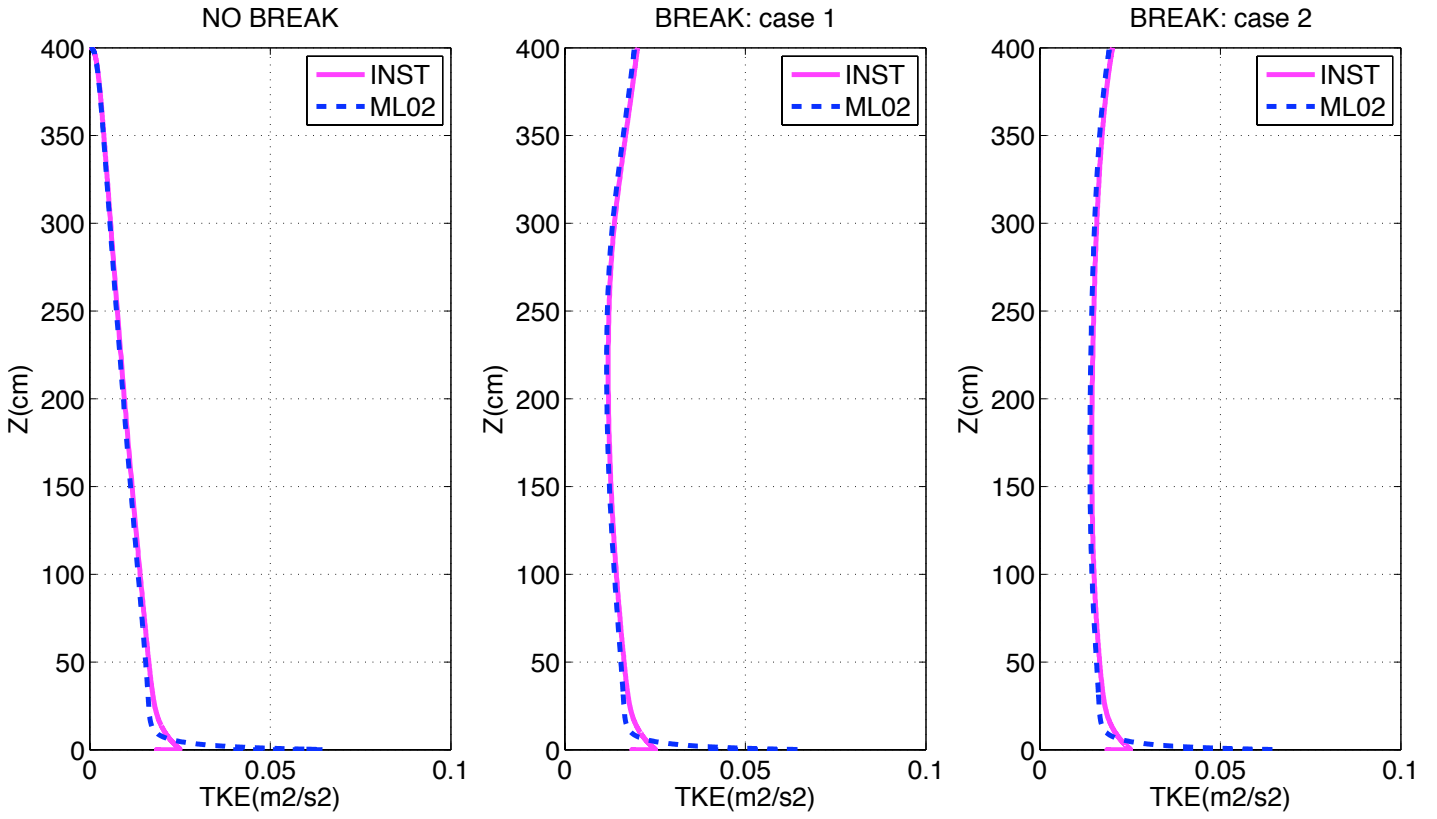


FIG. 4. Comparison of TKE vertical profiles for cases with and without waves breaking at the surface (NO BREAK: without waves breaking, BREAK: case 1 and 2 are for $\delta \simeq 1$ m and for $\delta \simeq 3$ m, respectively). Results given by the phase-resolving case (INST) are compared with the results given by the phase-averaged case (ML02).

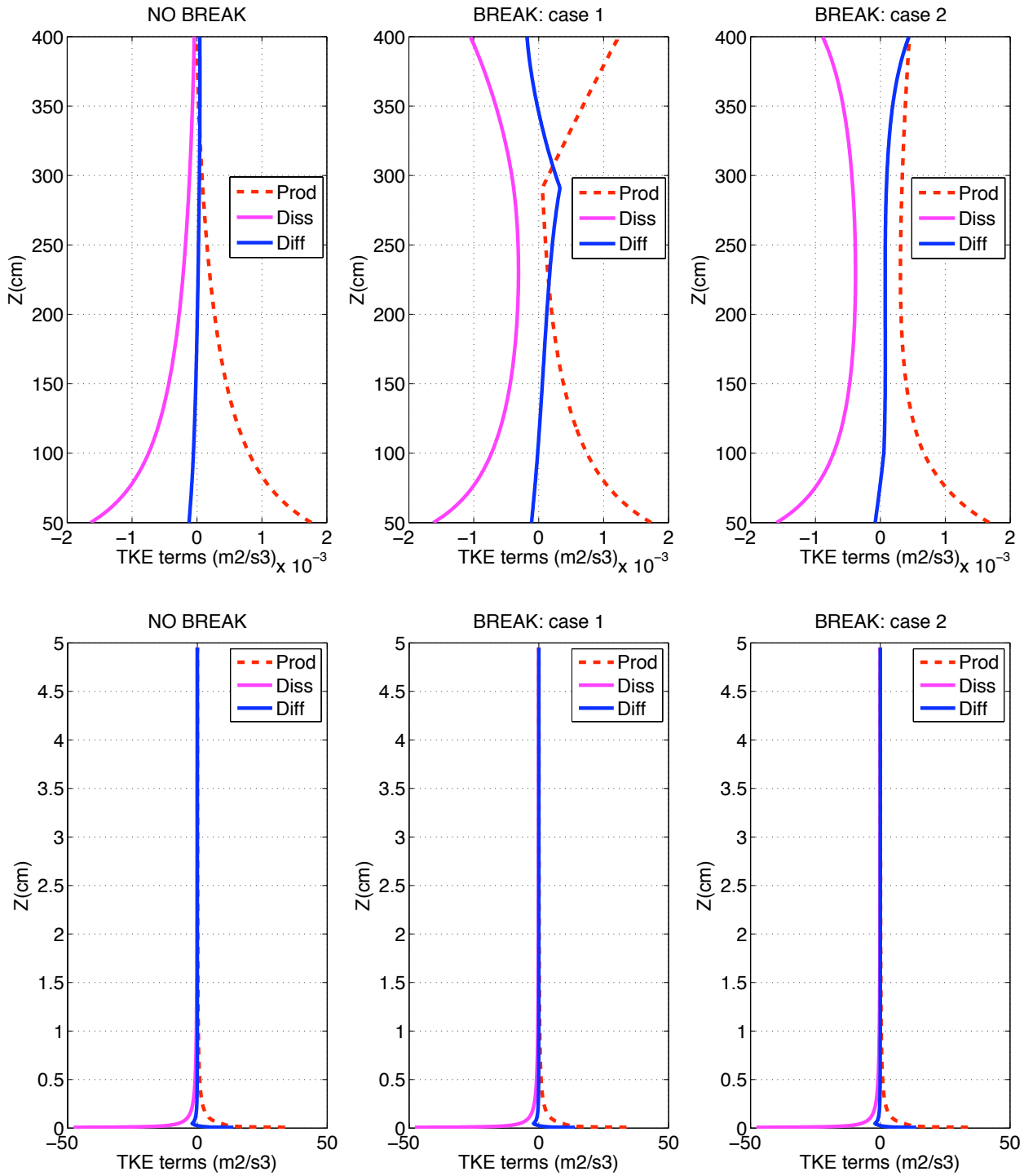


FIG. 5. TKE budget for the ML02 parameterization. The production terms (Prod), the dissipation terms (Diss) and the diffusion terms (Diff) are plotted as a function of depth. The top row shows the entire water column down to a depth of fifty centimeters. The bottom row shows the first five centimeters. Cases with and without wave breaking at the surface are displayed.

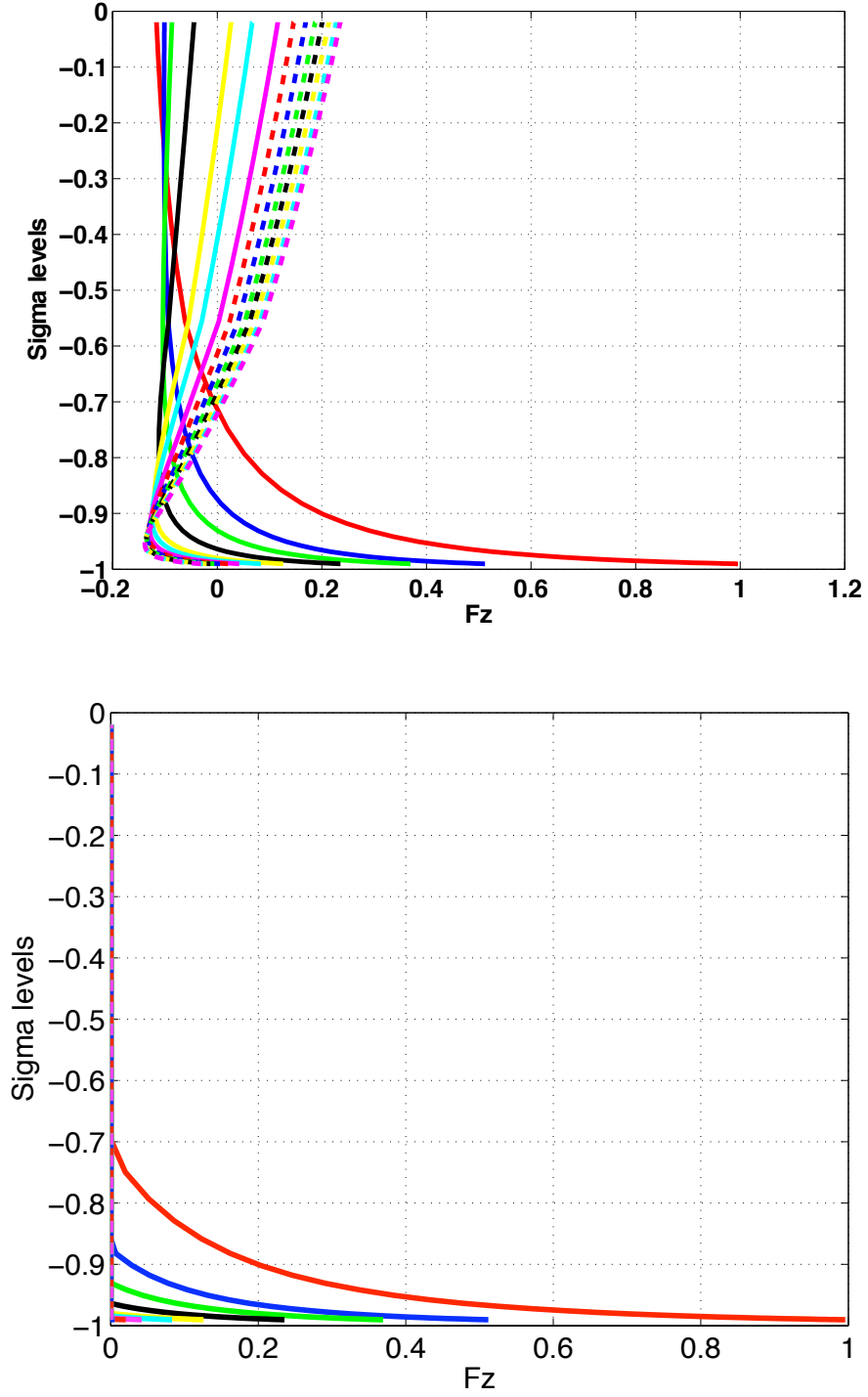


FIG. 6. F_{2z} function for different cross-shore positions. The original F_{2z} function given by ML02 (top row) and our modified function (bottom row).

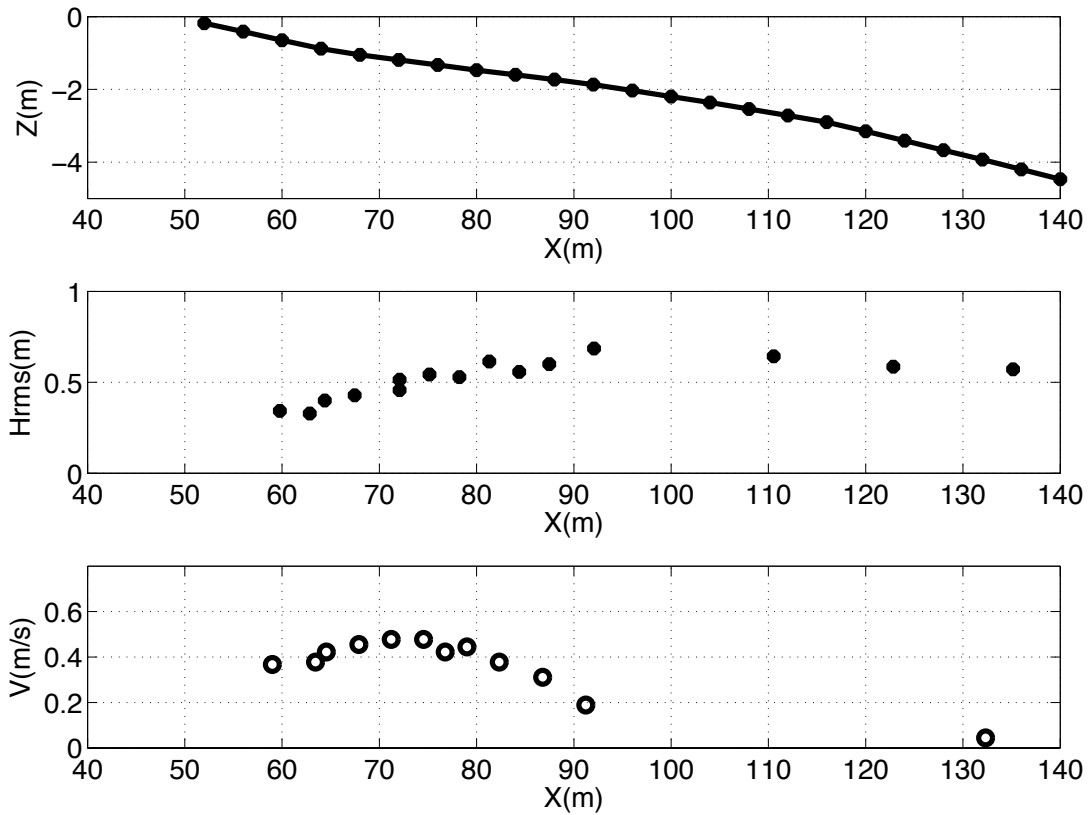


FIG. 7. Cross-shore profiles of bathymetry (top row), root mean square significant wave height (middle row) and barotropic longshore current (bottom row). All these profiles come from measurements made during the NSTS experiment.

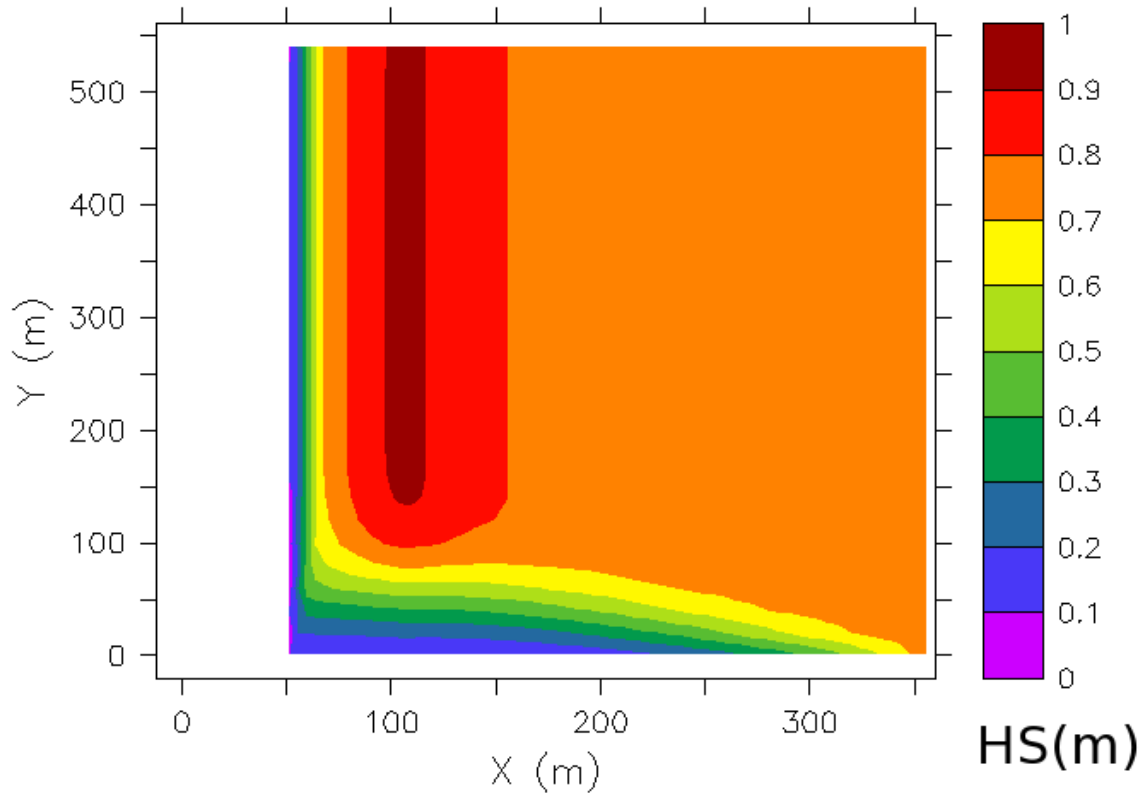


FIG. 8. Map of the significant wave height computed by WAVEWATCH III. The gray zone shows the computational domain used for the hydrodynamic model (MARS3D).

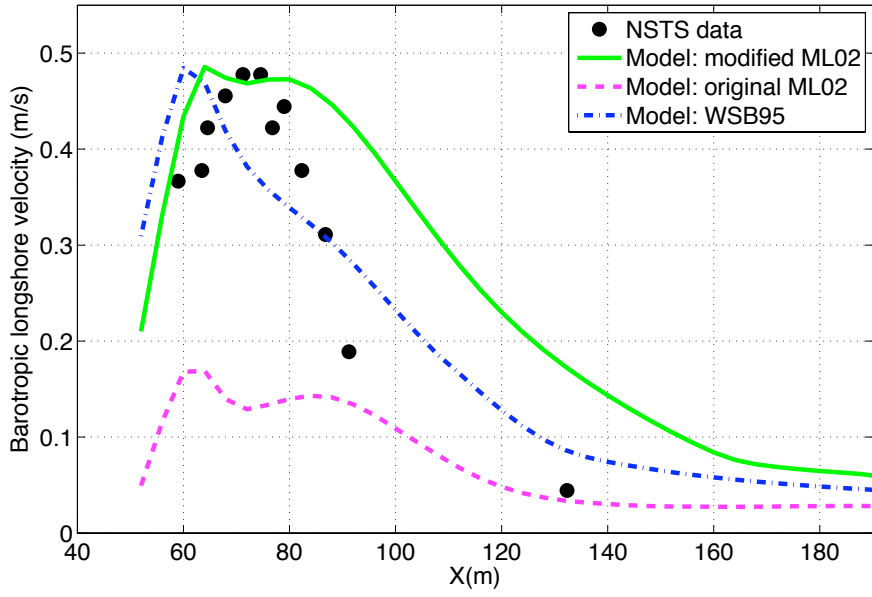
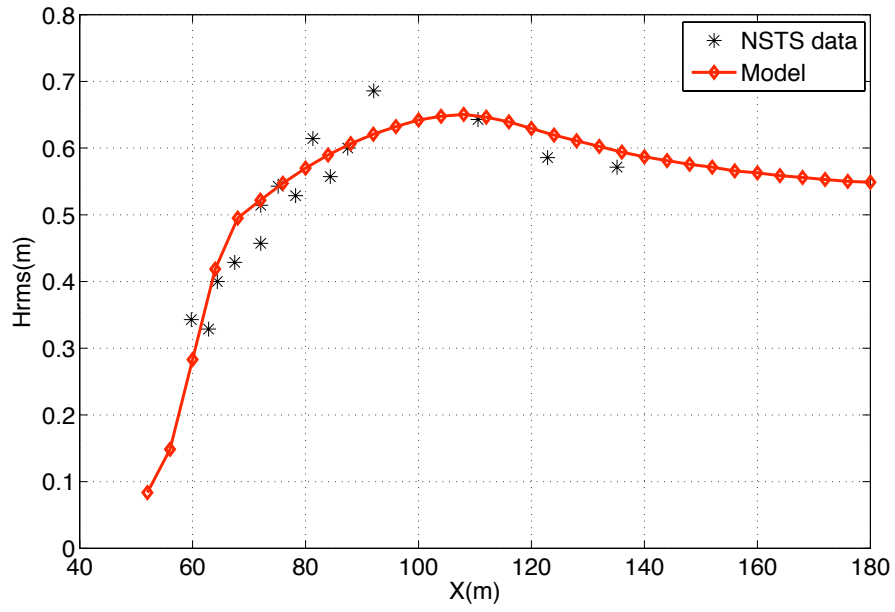


FIG. 9. Comparison between observational data and the model for the significant wave height (top row) and the barotropic longshore current (bottom row), with results from different parameterizations.

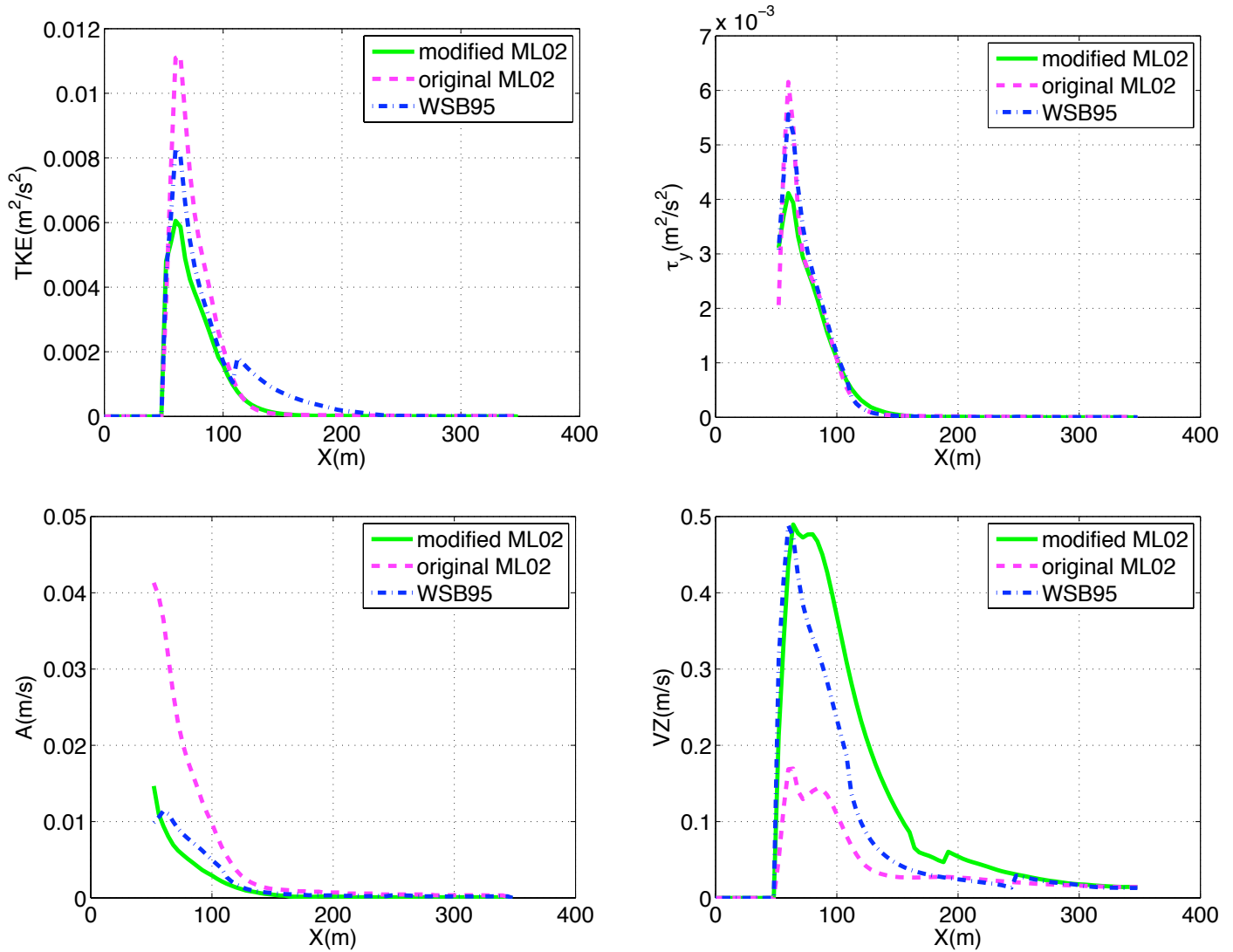


FIG. 10. Comparison between the modified ML02, the original ML02 and the WSB95 parameterizations for TKE (top row, left panel), the y-component of the bottom shear stress (top row, right panel), the term A (bottom row, left panel) and the 3D longshore velocity near the bottom (bottom row, right panel).

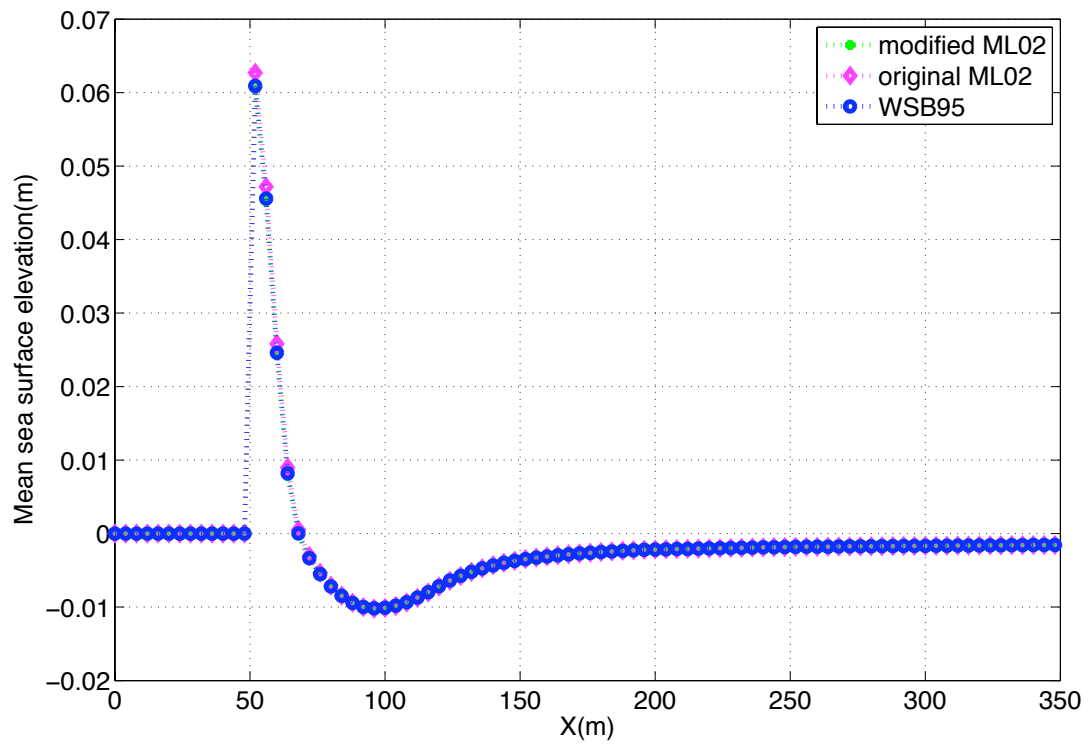


FIG. 11. Comparison of the mean sea surface elevation for the modified ML02, the original ML02, and the WSB95 parameterizations.